Application of Dynamic Mode Decomposition to Exponential Experiment for Spatial Decay Constant Determination

Toshihiro Yamamoto[a*], Hiroki Sakamoto[b]

[a]*Institute for Integrated Radiation and Nuclear Science, Kyoto University, 2 Asashiro Nishi, Kumatori-cho, Sennan-gun, Osaka, 590-0494, Japan*
[b]*Independent researcher, Radiation Dose Analysis and Evaluation Network, 4-13-14, Kokubunji-shi, Tokyo, 185-0001, Japan*

Abstract

When measuring the fundamental mode decay constant γ in an exponential experiment, it is difficult to extract the fundamental mode from a measured neutron flux distribution that is contaminated by many higher harmonics. Dynamic mode decomposition (DMD), which is intended for time-varying system analyses, is applied to the eigendecomposition of a three-dimensional flux distribution by viewing a series of two-dimensional flux profiles at horizontal planes as snapshots of a time-varying system. Through DMD, a fundamental mode can be extracted accurately from limited measured data that are largely contaminated by higher harmonics. The DMD yields a biased γ-eigenvalue if the statistical fluctuation of measured data is considered, and the bias is adjusted through a numerical simulation of an exponential experiment. Bootstrapping is employed for resampling the measured data from an exponential experiment. Ultimately, several measurements for an exponential experiment are closely simulated by bootstrap samples from a limited number of measurements.

Keywords: Gamma-eigenvalue; Exponential experiment; Higher harmonics; Dynamic mode decomposition; Bootstrapping

1. Introduction

In a nuclear fuel assembly where the horizontal buckling is larger than the axial (vertical) buckling and the material composition is vertically uniform, the asymptotic neutron flux decays

* Corresponding author. Tel:+81 72 451 2414
E-mail address: yamamoto.toshihiro.8u@kyoto-u.ac.jp (T. Yamamoto)

vertically from the neutron source according to an exponential function, $\exp(-\gamma z)$. The spatial decay constant, γ, is closely related to the subcriticality of the assembly. Similar to the prompt neutron time decay constant α, γ is an important factor for ensuring nuclear criticality safety in a nuclear fuel facility (Suzaki, 1991). The measured decay constant γ can be used as an indicator to benchmark nuclear criticality analysis codes. Suzaki et al. (1995, 1999) identified γ-values of PWR and BWR spent fuel assemblies by performing exponential experiments in spent fuel storage pools. The measured values contributed to validating the criticality safety analysis methods for spent fuels.

While the decay constant that is required to be measured in an exponential experiment is a fundamental mode eigenvalue, the measured flux distribution is the sum of a large number of higher harmonics. A formidable difficulty faced in an exponential experiment is the extraction of the fundamental mode eigenvalue from the flux distribution that is contaminated by higher harmonics. Yamamoto et al. (2003) developed an analysis method to expand the horizontal flux distribution into a series of eigenfunctions. The method was applied to an exponential experiment performed in the tank-type critical assembly (TCA) (Tsuruta et al., 1978) of the former Japan Atomic Energy Research Institute. It provides useful information on the influence of each higher harmonic on the measured results in an exponential experiment.

Similar problems regarding the effect of higher harmonics are encountered when measuring the time-decay constant α using the pulsed neutron method. Immediately after the generation of a pulsed neutron, the time decay of the neutron flux is influenced by a large number of higher harmonics. Recently, a new method was developed to decompose the time-decaying flux into important eigenfunctions based on the dynamic mode decomposition (DMD) method (McClarren, 2019; Hardy et al., 2019). The DMD method (Schmid, 2010; Kutz et al., 2016) was originally developed in the fluid dynamics field as a mathematical technique for decomposing complex fluid flows into a simple representation based on spatiotemporal coherent structures. DMD is advantageous because it is an equation-free, data-driven method that can enable precise decomposition of a complex system into spatiotemporal coherent structures.

The applications of DMD are concentrated on time-varying phenomena, such as fluid flows and pulsed neutron time decay. Some recent applications of DMD in the nuclear engineering field are published in (Abdo et al., 2019; McClarren and Haut, 2020; Di Ronco et al., 2020). A unique and significant application of DMD in the nuclear engineering field is the acceleration of the power iteration method for *k*-eigenvalue calculations (Roberts, et al., 2019). DMD was applied to the power iteration method by viewing successive iterations of the fission source distribution as snapshots of a time-varying system. Similarly, through substitution of the temporal evolution in DMD with the spatial propagation in an exponential experiment and viewing of horizontal flux profiles as snapshots of a time-varying phenomenon, DMD is expected to serve as a viable tool for extraction of a fundamental mode γ-eigenvalue from a measured flux distribution. With this context, the objective of this study is to examine the applicability of DMD to higher harmonic decomposition in an exponential experiment.

The remainder of this paper is organized as follows. Section 2 provides a brief review of the authors' conventional method of higher-harmonic decomposition in an exponential experiment. Section 3 presents an explanation for the application of DMD to the exponential experiment, and Section 4 presents numerical examples. In Section 5, the effect of statistical measurement uncertainty in an exponential experiment on the γ-eigenvalue is discussed, and a method to account for this effect is proposed. The final section presents the conclusions of the study.

2. Exponential experiment and higher harmonics analysis

The exponential experiment is a well-known classical technique used to identify the degree of subcriticality (Suzaki, 1991). The higher-harmonic analysis method for an exponential experiment was previously developed by one of the authors (Yamamoto, et al., 2003). This section briefly revisits the higher-harmonic analysis method. Because the calculation code of the higher-harmonic decomposition used in this study is based on the diffusion approximation, the theory presented in this study uses diffusion equations. To calculate a fundamental mode γ-eigenvalue using the Monte Carlo method, the reader may refer to the studies of (Yamamoto and Miyoshi, 2003; Yamamoto, 2012; Yamamoto and Sakamoto, 2019a).

A multi-group, two-dimensional diffusion equation for the *m*th-mode γ-eigenvalue is given as follows:

$$\boldsymbol{M}_g(\boldsymbol{r})\phi_g^m(\boldsymbol{r}) = \gamma_m^2 D_g(\boldsymbol{r})\phi_g^m(\boldsymbol{r}), \quad m = 0,1,2,\cdots, \tag{1}$$

where ϕ_g^m is the *m*th-mode eigenfunction of the neutron flux in the energy group g, D_g is the diffusion coefficient, γ_m is the *m*th-mode γ-eigenvalue, and $\boldsymbol{r}$ is the position vector in the horizontal plane. The left-hand side of Eq. (1) is defined as follows:

$$\boldsymbol{M}_g(\boldsymbol{r})\phi_g^m(\boldsymbol{r}) \equiv -\nabla D_g(\boldsymbol{r})\cdot\nabla\phi_g^m(\boldsymbol{r}) + \Sigma_{ag}(\boldsymbol{r})\phi_g^m(\boldsymbol{r}) + \sum_{\substack{g'=1\\ g\neq g'}}^{G}\Sigma_s^{g\to g'}(\boldsymbol{r})\phi_g^m(\boldsymbol{r})$$

$$-\chi_g\sum_{g'=1}^{G}\nu\Sigma_{fg'}(\boldsymbol{r})\phi_{g'}^m(\boldsymbol{r}) - \sum_{\substack{g'=1\\ g\neq g'}}^{G}\Sigma_s^{g'\to g}(\boldsymbol{r})\phi_{g'}^m(\boldsymbol{r}), \quad g = 1,2,\cdots,G, \tag{2}$$

where Σ_{ag} is the absorption cross section, $\Sigma_s^{g'\to g}$ is the scattering cross section from group g' to g, $\nu\Sigma_{fg}$ is the production cross section, and χ_g is the fission spectrum. Similarly, the adjoint diffusion equation in Eq. (2) is given as follows:

$$\boldsymbol{M}_g^*(\boldsymbol{r})\psi_g^n(\boldsymbol{r}) = \gamma_n^2 D_g(\boldsymbol{r})\psi_g^n(\boldsymbol{r}), \quad n = 0,1,2,\cdots, \tag{3}$$

where ψ_g^n is the *n*th-mode eigenfunction of the adjoint flux. The left-hand side of Eq. (3) is defined as follows:

$$\boldsymbol{M}_g^*(\boldsymbol{r})\psi_g^n(\boldsymbol{r}) \equiv -\nabla D_g(\boldsymbol{r})\cdot\nabla\psi_g^n(\boldsymbol{r}) + \Sigma_{ag}(\boldsymbol{r})\psi_g^n(\boldsymbol{r}) + \sum_{\substack{g'=1\\ g\neq g'}}^{G}\Sigma_s^{g'\to g}(\boldsymbol{r})\psi_g^n(\boldsymbol{r})$$

$$-\nu\Sigma_{fg}(\boldsymbol{r})\sum_{g'=1}^{G}\chi_{g'}\psi_{g'}^n(\boldsymbol{r}) - \sum_{\substack{g'=1\\ g\neq g'}}^{G}\Sigma_s^{g\to g'}(\boldsymbol{r})\psi_{\mathrm{g}'}^n(\boldsymbol{r}). \tag{4}$$

A three-dimensional neutron flux distribution formed in an exponential experiment is given by the solution of the fixed source problem as follows:

$$\boldsymbol{M}_g(\boldsymbol{r},z)\phi_g^s(\boldsymbol{r},z) = S(\boldsymbol{r},z), \tag{5}$$

where ϕ_g^s is the neutron flux in the fixed source problem, $S(\boldsymbol{r},z)$ is the neutron source density at $(\boldsymbol{r},z)$, and $M_g(\boldsymbol{r},z)$ is the same as $M_g(\boldsymbol{r})$ except that $(\boldsymbol{r})$ in Eq. (2) is replaced with $(\boldsymbol{r},z)$. Using the eigenfunctions of Eq. (1), the three-dimensional neutron flux distribution is expanded as follows:

$$\phi_g^s(\boldsymbol{r},z)=\sum_{m=0}^{\infty}a_m(z)\phi_g^m(\boldsymbol{r}), \tag{6}$$

where $a_m(z)$ is the expansion coefficient of the *m*th eigenfunction. $\phi_g^m(\boldsymbol{r})$ and $\psi_g^n(\boldsymbol{r})$ have the following orthogonality relations:

$$\langle\psi_g^n(\boldsymbol{r})D_g(\boldsymbol{r})\phi_g^m(\boldsymbol{r})\rangle=0 \quad \text{for } m\neq n \text{ and } \gamma_m\neq\gamma_n, \tag{7}$$

$$\langle\psi_g^n(\boldsymbol{r})D_g(\boldsymbol{r})\phi_g^m(\boldsymbol{r})\rangle\neq0 \quad \text{for } m=n\,. \tag{8}$$

where the angle brackets represent the integration over the entire volume and energy groups. Using orthogonality relations, the expansion coefficient is given as follows:

$$a_m(z)=\frac{\langle\psi_g^m(\boldsymbol{r})D_g(\boldsymbol{r})\phi_g^s(\boldsymbol{r},z)\rangle}{\langle\psi_g^m(\boldsymbol{r})D_g(\boldsymbol{r})\phi_g^m(\boldsymbol{r})\rangle}\,. \tag{9}$$

When the *m*th and *n*th eigenvalues are equal and degenerate, the expansion coefficients of both eigenfunctions are given by the solution of the following simultaneous equations:

$$\langle\psi_g^n(\boldsymbol{r})D_g(\boldsymbol{r})\phi_g^s(\boldsymbol{r},z)\rangle=a_m(z)\langle\psi_g^n(\boldsymbol{r})D_g(\boldsymbol{r})\phi_g^m(\boldsymbol{r})\rangle+a_n(z)\langle\psi_g^n(\boldsymbol{r})D_g(\boldsymbol{r})\phi_g^n(\boldsymbol{r})\rangle, \tag{10}$$

$$\langle\psi_g^m(\boldsymbol{r})D_g(\boldsymbol{r})\phi_g^s(\boldsymbol{r},z)\rangle=a_m(z)\langle\psi_g^m(\boldsymbol{r})D_g(\boldsymbol{r})\phi_g^m(\boldsymbol{r})\rangle+a_n(z)\langle\psi_g^m(\boldsymbol{r})D_g(\boldsymbol{r})\phi_g^n(\boldsymbol{r})\rangle. \tag{11}$$

3. DMD for exponential experiment

DMD is a dimensionality reduction method widely used in many fields of application, and the details thereof are presented extensively in the literature. Here, the outline of DMD that focuses on application to an exponential experiment is described. Among the many variants of DMD, the DMD algorithm in this study relies on the description in Chapter 1 of the report by (Kutz et al., 2016).

A schematic overview of the exponential experiment is illustrated in Fig. 1. We assume that we have *n* measured data (e.g., neutron count rate) in each horizontal plane (snapshot), and the total number of horizontal planes is *m*. The set of the *n*-measured data at the *j*th horizontal plane constitutes an *n*-dimensional column vector:

$$\mathbf{x}_j=\left[x_{1,j}\ \ x_{2,j}\ \ldots\ x_{i,j}\ \ldots x_{n,j}\ \right]^T, \tag{12}$$

where $x_{i,j}$ is the *i*th measured data in the *j*th horizontal plane. Each $\mathbf{x}_j$ corresponds to a snapshot in the dynamic mode. In this study, the DMD algorithm was designed to collect the vector $\mathbf{x}_j$ at regularly spaced intervals Δz in the vertical direction. Next, we define the two matrices as follows:

$$\mathbf{X} = \left[\mathbf{x}_1\ \mathbf{x}_2 \dots \mathbf{x}_j \dots \mathbf{x}_{m-1}\right], \tag{13}$$

$$\mathbf{X}' = \left[\mathbf{x}_2\ \mathbf{x}_3 \dots \mathbf{x}_j \dots \mathbf{x}_m\right]. \tag{14}$$

Both $\mathbf{X}$ and $\mathbf{X}'$ are $n \times (m-1)$ matrices. We assume that there exists a matrix $\mathbf{A}$ that linearly connects $\mathbf{X}$ to $\mathbf{X}'$ as follows:

$$\mathbf{X}' \approx \mathbf{A}\mathbf{X}. \tag{15}$$

The best-fit $n \times n$ matrix $\mathbf{A}$ is given by as follows:

$$\mathbf{A} = \mathbf{X}'\mathbf{X}^{\dagger}, \tag{16}$$

where $\dagger$ indicates the Moore−Penrose pseudoinverse. We perform a singular value decomposition of $\mathbf{X}$ as follows:

$$\mathbf{X} = \mathbf{U}\mathbf{\Sigma}\mathbf{V}^{*}, \tag{17}$$

where $*$ denotes the conjugate transpose, and $\mathbf{U} \in \mathbb{C}^{n\times n}$; $\mathbf{\Sigma} \in \mathbb{C}^{n\times n}$; $\mathbf{V} \in \mathbb{C}^{(m-1)\times n}$. As shown in the numerical examples in Section 4, performing a low-rank truncation to $\mathbf{U}$, $\mathbf{\Sigma}$, and $\mathbf{V}$ might yield better solutions than when using the full-rank matrices. After a low-rank $r(\leq \min(n, m-1))$ is chosen, $\mathbf{X}$ is approximated by the truncated matrices:

$$\mathbf{X} \approx \mathbf{U}_{\mathrm{r}}\mathbf{\Sigma}_{\mathrm{r}}\mathbf{V}_{\mathrm{r}}^{*}, \tag{18}$$

where $\mathbf{U}_{\mathrm{r}} \in \mathbb{C}^{n\times r}, \mathbf{\Sigma}_{\mathrm{r}} \in \mathbb{C}^{r\times r}$, and $\mathbf{V}_{\mathrm{r}} \in \mathbb{C}^{(m-1)\times r}$. $\mathbf{U}_{\mathrm{r}}$ and $\mathbf{V}_{\mathrm{r}}$ are obtained by considering the first r rows from $\mathbf{U}$ and $\mathbf{V}$, respectively. $\mathbf{\Sigma}_{\mathrm{r}}$ is obtained by considering the first r rows and r columns from $\mathbf{\Sigma}$. After $\mathbf{U}_{\mathrm{r}}, \mathbf{\Sigma}_{\mathrm{r}}$, and $\mathbf{V}_{\mathrm{r}}$ are obtained, the pseudoinverse of $\mathbf{X}$ is given as follows:

$$\mathbf{X}^{\dagger} = \mathbf{V}_{\mathrm{r}}\mathbf{\Sigma}_{\mathrm{r}}^{-1}\mathbf{U}_{\mathrm{r}}^{*}. \tag{19}$$

The rank-reduced representation of the $n \times n$ matrix $\mathbf{A}$ is given by an $r \times r$ matrix as follows:

$$\widetilde{\mathbf{A}} = \mathbf{U}_{\mathrm{r}}^{*}\mathbf{A}\mathbf{U}_{\mathrm{r}} = \mathbf{U}_{\mathrm{r}}^{*}\mathbf{X}'\mathbf{V}_{\mathrm{r}}\mathbf{\Sigma}^{-1}. \tag{20}$$

The matrix $\widetilde{\mathbf{A}}$, which represents a similarity transformation of $\mathbf{A}$, has the same eigenvalues as $\mathbf{A}$. Next, the eigendecomposition of $\widetilde{\mathbf{A}}$ is performed as follows:

$$\widetilde{\mathbf{A}}\mathbf{W} = \mathbf{W}\mathbf{\Lambda}, \tag{21}$$

where columns of $\mathbf{W}$ are the leading r eigenvalues of $\mathbf{A}$ inferred from $\widetilde{\mathbf{A}}$, and $\mathbf{\Lambda}$ is a diagonal matrix whose diagonal components are eigenvalues λ_k corresponding to $\mathbf{W}$. The eigenvalues of $\mathbf{A}$ are the diagonal components of $\mathbf{\Lambda}$, and the eigenvectors of $\mathbf{A}$ are given by the columns of $\mathbf{\Phi}$:

$$\mathbf{\Phi} = \mathbf{X}'\mathbf{V}_{\mathrm{r}}\mathbf{\Sigma}_{\mathrm{r}}^{-1}\mathbf{W}, \tag{22}$$

where the modes are called "exact DMD modes" (Kutz et al., 2016).

Here, we suppose that the evolution of the vector $\mathbf{x}$ can be approximated by the differential equation:

$$\frac{d\mathbf{x}(z)}{dz} = \mathbf{B}\mathbf{x}, \tag{23}$$

where $\mathbf{B}$ is the linear mapping operator and also the matrix in the continuous-space dynamics. Meanwhile, as shown in Eq. (15), the vector $\mathbf{X}$ is connected to $\mathbf{X}'$ by the local linear approximation $\mathbf{X}' \approx \mathbf{A}\mathbf{X}$. The solution to Eq. (23) is given by as follows:

$$\mathbf{x}(z) = \mathbf{x}(\mathbf{0})\boldsymbol{e}^{\mathbf{B}z}. \tag{24}$$

The matrix $\mathbf{A}$ corresponds to the discrete-space approximation to $\boldsymbol{e}^{\mathbf{B}\Delta z}$. The continuous-space eigenvalue, i.e., the γ-eigenvalue, is related to the discrete eigenvalue λ_k of $\mathbf{A}$ as follows:

$$\lambda_k = \exp(\gamma_k \Delta z). \tag{25}$$

Using the eigenvalues and eigenvectors of $\mathbf{A}$, the measured data as a continuous function of the vertical position z is approximated as follows:

$$\mathbf{x}(z) \approx \mathbf{\Phi} \exp(\mathbf{\Gamma} z)\, \mathbf{b}, \tag{26}$$

where

$$\mathbf{b} = [b_1\ b_2\ \ldots\ b_k\ \ldots\ b_r\ ]^T, \tag{27}$$

b_k is the amplitude of the kth mode at the first horizontal plane, and $\mathbf{\Gamma}$ is an $r \times r$ diagonal matrix with the kth entry equal to

$$\gamma_k = \frac{\ln(\lambda_k)}{\Delta z}. \tag{28}$$

Because $\mathbf{x}_1 = \mathbf{x}(0) = \mathbf{\Phi}\mathbf{b}$, the amplitude vector at the first horizontal plane is given as follows:

$$\mathbf{b} = \mathbf{\Phi}^{\dagger}\mathbf{x}_1, \tag{29}$$

where $\mathbf{\Phi}^{\dagger}$ is the Moore−Penrose pseudoinverse of $\mathbf{\Phi}$.

4. Application of DMD to exponential experiment

4.1 Vertical flux distribution and decay constant

The DMD method described in Section 3 was applied to a numerical model simulating an exponential experiment in the TCA (Tsuruta et al., 1978; Yamamoto et al., 2003). The numerical model was composed of an 11×11 rectangular array of 2.60 wt% enriched UO_2 fuel rods immersed in a light water moderator/reflector. The center-to-center spacing of the fuel rods was 1.956 cm, and the outer diameter of the aluminum cladding was 1.42 cm, which corresponded to a moderator-to-fuel ratio of 1.83. The horizontal and vertical configurations of the model are shown in Figs 2 and 3, respectively.

This study used the diffusion code RHEINGOLD (Resolution of Higher order EIgenvalues for Neutronic Gamma, Omega, and Lambda mode Diffusion theory) for eigendecomposition of the two-dimensional horizontal flux distribution in the exponential experiment (Yamamoto, et al., 2003; Yamamoto and Sakamoto, 2019b). Because of the limitation of the matrix size in RHEINGOLD, diffusion calculations were performed with two-energy group constants. The group constants of the homogenized fuel rod array and water reflector are listed in Table 1. The horizontal domain was discretized into a 67 × 67 mesh, as shown in Fig. 2. The k_{eff} of this two-dimensional system with zero vertical buckling was 0.8823. The three-dimensional flux distribution formed in the exponential experiment was calculated using the diffusion code CITATION (Fowler et al., 1971). The regularly spaced mesh interval Δz in the vertical direction was 1 cm. A standard extrapolated boundary condition was imposed on all external boundaries (i.e., $-D\nabla\phi/\phi = 0.4692$). The location of a neutron source that solely emitted fast neutrons is shown in Figs 2 and 3. The neutron source was intentionally placed off-center along the diagonal line to excite the asymmetric higher harmonics. Thus, the flux distribution largely deviated from the fundamental mode distribution, particularly near the neutron source, because of the excited higher harmonics. This proved to be a challenging problem for DMD to extract the fundamental mode from the flux distribution.

Table 1 Group constants of fuel rod array and water reflector

	Fuel rod array	Water reflector
D_1 (cm)	1.02294	0.905414
D_2(cm)	0.197177	0.125647
$\nu\Sigma_{f1}$ (cm^{-1})	0.00643278	0
$\nu\Sigma_{f2}$(cm^{-1})	0.155089	0
Σ_{a1} (cm^{-1})	0.00812186	0.000460058
Σ_{a2}(cm^{-1})	0.097414	0.0188813
$\Sigma_s^{1\to2}$ (cm^{-1})	0.0225208	0.0584208

Because neutron detectors are sensitive to thermal neutrons, this study discusses the results of thermal neutron flux. The thermal flux distributions in the *z*-direction above the neutron source, which were calculated by solving the fixed source problem of CITATION code, are shown in Fig. 4. The locations of the flux distributions in the *x*-*y* plane (A, B, and C) are shown in Fig. 5. Because a logarithmic scale is used for the vertical axis (flux) in Fig. 4, the flux linearly decreases with the horizontal axis (distance) if the flux decays with a single decay constant (i.e., fundamental mode decay constant). However, the flux distribution near the neutron source (A) is convex downwards up to approximately 40 cm from the neutron source, which is caused by the positive higher harmonics. The flux distribution far from the neutron source (C) is convex upwards, which is caused by the negative higher harmonics. At the center of the fuel rod array (B), the flux mostly decreases with a single decay constant, except near the neutron source and upper boundary. This is because position B is the node of asymmetric higher harmonics, and the effect of the higher harmonics is minor. The rapid flux decline above 140 cm from the neutron source was caused by the effect of the boundary condition of the upper surface. Between 60 cm and 100 cm, the flux decayed with a single decay constant regardless of the horizontal position. The local decay constant at each vertical position is calculated by two adjacent fluxes as follows:

$$\gamma = -\frac{\ln(\phi_{i+1}) - \ln(\phi_i)}{\Delta z}, \tag{30}$$

where ϕ_i is the thermal flux at mesh point *i*. The local decay constants at positions A, B, and C are shown in Fig. 6. The exact fundamental mode decay constant γ_0 calculated using the RHEINGOLD code was 0.07113 cm^{-1}. While the local decay constants are different from γ_0 in the lower part, it can be accurately reproduced by fitting a vertical flux distribution at A and C in the range of 60–100 cm. The best-fit range for determining γ_0 extends wider at the center position B. However, in an actual exponential experiment, the neutron detection efficiency declines due to the decrease of neutron counts as the detection position becomes far from the neutron source. A neutron detector may not be inserted within the fuel-rod array. The detection is not always possible in the range where the fundamental mode decay constant can be measured. There may be some

occasions where only the flux distributions highly contaminated by higher harmonics are available for an exponential experiment. This study attempts to extract the fundamental-mode decay constant from flux distributions that are largely affected by higher harmonics.

4.2 Resolution of higher harmonics in γ-eigenvalue mode

The γ-eigenvalue mode higher-harmonic analysis was performed for the two-dimensional subcritical system shown in Fig. 2 using the RHEINGOLD code. The γ-eigenvalue mode diffusion equations in Eqs. (1) and (3) were discretized using a finite difference approximation to derive matrix eigenvalue equations. The matrix eigenvalue equations were solved using the double QR method to obtain the eigenvalues and eigenfunctions of the higher harmonics (Anderson et al., 1999). The finite difference scheme in RHEINGOLD is the same as that for CITATION code. Thus, the fundamental mode γ-eigenvalue is equal to the result of the buckling search calculation in CITATION code. The γ-eigenvalues and a schematic of the flux distributions up to the 5th-higher harmonics are shown in Fig. 7. The two-dimensional flux distribution ϕ_s in the *x*-*y* plane used in Eq. (9) was taken out from the three-dimensional flux distribution calculated using the fixed source calculation of CITATION code. The vertical location of ϕ_s was 5 cm above the neutron source, as shown in Fig. 3. Using Eqs. (6) and (9), ϕ_s is decomposed into a series of eigenfunctions. Fig. 8 shows the thermal flux distributions of ϕ_s, fundamental mode, and higher harmonics up to 4th order along the diagonal line (red dotted line) in Fig. 2. At this elevation, not far from the neutron source, the higher harmonics are dominant over the fundamental mode. Fig. 9 shows the vertical distributions of the thermal fluxes up to the 4th order at position A. The contribution of the higher harmonics decayed with the vertical distance from the neutron source. Beyond approximately 50 cm from the neutron source, the thermal flux distribution is mostly dominated by the fundamental mode.

4.3 Resolution of higher harmonics using DMD

4.3.1 Use of many data points in horizontal direction

The three-dimensional flux distribution calculated using the fixed source problem of

CITATION code was decomposed using the DMD method. Because the objective of an exponential experiment is to find the fundamental-mode γ-eigenvalue, this study focuses on finding the fundamental mode eigenvalue and eigenfunction as accurately as possible, rather than finding the higher harmonics. When performing an exponential experiment, there can be an unlimited number of combinations of measurement points in a three-dimensional space. Thus, this study does not attempt to find an optimal experimental condition for determining the fundamental mode eigenvalue. Instead, this study focuses on how the fundamental mode eigenvalue and eigenfunction can be reproduced under certain experimental conditions. Throughout this study, the vertical range of the neutron flux used for DMD was between 5 cm and 34 or 35 cm from the neutron source. The upper bound of the vertical range varied depending on the number of data points. Because the mesh interval was 1 cm in the vertical direction, the number of data points was 30 at most in the direction. The vertical range is the yellow-hatched area in Figs. 4 and 6.

In the first numerical example, the data points of the thermal neutron flux in the *x*-*y* direction were all mesh points along the diagonal (red dotted line) and horizontal (blue dotted line) lines in Fig. 2. The total number of data points in the *x*-*y* direction was 133 (67 + 66). Thus, matrix $\mathbf{X}$ (and $\mathbf{X}'$) defined by Eq. (13) (and Eq. (14), respectively) has dimensions of $133 \times (30-1)$. According to the DMD algorithm described in Section 3, the γ-eigenvalues and eigenfunctions were obtained using the eigendecomposition defined by Eq. (21). To assess the quality of the fundamental mode reproduction, the convergence of the DMD solution was measured using the norm:

$$\varepsilon = \sum_{i=1}^{M} \left(a_0 \phi_i^0 - b_k \Phi_{k,i} \right)^2, \tag{31}$$

where *i* is the index of the data point in the *x*-*y* direction, *M* is the total number of data points (i.e., 133), $a_0 \phi_i^0$ is the fundamental mode component decomposed from the flux distribution at the lowest horizontal plane (5 cm from the neutron source), and *k* is the row number corresponding to the fundamental mode in the amplitude vector $\mathbf{b}$ (defined by Eq. (29)) and matrix $\mathbf{\Phi}$ (defined by Eq. (22)). While $\widetilde{\mathbf{A}}$ (defined by Eq. (20)) has a full rank of at most 29, the smallest norm ε was attained when the rank $r = 23$. The DMD solution captured feasible eigenvalues up to the

third-higher harmonic. The second-higher harmonic was not captured because the neutron source was placed at the node of the second-higher harmonics. The eigenvalues of $\tilde{\mathbf{A}}$ with $r = 23$ up to the third-higher harmonic were compared with the exact values obtained by the RHEINGOLD code in Table 2. DMD yielded a precise reproduction of the exact eigenvalues of the fundamental mode and first-higher harmonic. The eigenvalues of the third-higher harmonic did not correspond well when compared to the first two eigenvalues. The eigenfunctions along the diagonal line at the lowest horizontal plane are shown in Fig. 10 (fundamental mode), Fig. 11 (first-higher harmonic), and Fig. 12 (third-higher harmonic). The solutions from RHEINGOLD are also shown in these figures for comparison. Similar to the eigenvalues, the fundamental mode and first-higher harmonic eigenfunctions extracted from the DMD accurately matched the exact eigenfunctions. Although the DMD solution for the third-higher harmonic spatial distribution definitely deviated from the true solution, it roughly characterized the exact solution.

Another numerical example where the neutron source was placed at the node of the third-higher harmonic are presented in Appendix.

Table 2 Eigenvalues of DMD from matrix of 133 × 29 and $r = 23$

	Exact (cm^{-1})	DMD (cm^{-1})
γ_0	0.07113	0.07112
γ_1	0.1723	0.1724
γ_3	0.2324	0.2311
γ_4	0.2584	—
γ_5	0.2602	—

4.3.2 Use of limited number of data points

In an actual exponential experiment, the number of measurement points and measurement time must be limited owing to some experimental requirements. In particular, measurements within a fuel rod array are mostly impossible because a neutron detector can hardly be inserted within the fuel rod array, except in a water rod or thimble. Hence, most of the measurements must

be performed outside the fuel rod array. Given that the time required for an exponential experiment increases with the number of measurement points, an exponential experiment should be performed at a limited number of measurement points. Considering such limitations in an exponential experiment, 16 points outside the fuel rod array were chosen for the next numerical example, as indicated by the red circles in Fig. 5. The vertical range was again between 5 cm and 34 or 35 cm from the neutron source. The maximum number of data points in the vertical direction (snapshots) was 30 when all data points aligned at 1 cm intervals were used for DMD. However, the use of the maximum number of data points and finest vertical interval did not yield the most accurate eigenvalues from the DMD. The reason of this phenomenon can be hypothesized by considering the following factors. The fundamental mode can be accurately extracted from a fewer number of data points in a region where the fundamental mode is dominant over higher harmonics. On the other hand, too fine interval of the data points unnecessarily increases the influence of the undesired higher harmonics near the neutron source, which may cause the fundamental mode eigenvalue from the DMD deviate from the best solution. The vertical interval was changed from 1 to 6 cm, and the rank that yielded the best solution, i.e., the lowest ε defined by Eq. (31), was determined. The eigenvalues up to the third-higher harmonic for each interval are listed in Table 3, which shows that the best solutions were obtained with an interval of 3 or 4 cm regardless of losing the resolution in the vertical direction. The eigenfunctions along the diagonal line at the lowest horizontal plane are compared between the DMD solutions and exact solutions in Fig. 13 (fundamental mode), Fig. 14 (first-higher harmonic), and Fig. 15 (third-higher harmonic). The DMD solutions in these figures were for a vertical interval of 3 cm. While the first- and third-higher harmonics reproduced via DMD involved significant deviations from the exact solutions, the fundamental mode was accurately reproduced.

Table 3 Eigenvalues of DMD for vertical intervals from 1 to 6 cm

Interval	Vertical data points	Rank (full rank)	γ_0 (cm^{-1})	γ_1 (cm^{-1})	γ_3 (cm^{-1})
Exact	NA	NA	0.07113	0.1723	0.2324
1 cm	30	16 (16)	0.07131	0.1673	0.2270
2 cm	16	10 (15)	0.07119	0.1680	—*
3 cm	11	10 (10)	0.07119	0.1720	0.2211
4 cm	9	7 (8)	0.07117	0.1701	0.2377
5 cm	7	6 (6)	0.07114	0.1698	0.2408
6 cm	6	5 (5)	0.07120	0.1777	—*

*This mode was not extracted.

5. Estimation of true decay constant with DMD

5.1 Effect of measurement uncertainty

As described in the previous section, DMD was applied to the exact numerical solution of the neutron flux distribution in an exponential experiment. However, the measured values always entail certain statistical uncertainties. The neutron count N has a fractional standard deviation uncertainty of $1/\sqrt{N}$. In this section, the effect of this statistical uncertainty on the fundamental mode eigenvalue obtained by the DMD is examined. The numerical example in Section 4.3.2 was used for this test. All data points were in the water reflector, with a vertical interval of 2 cm. The matrix **X**, defined by Eq. (13), has dimensions of 16 × (16−1). It was assumed that all data in this matrix randomly varied around the true values according to the normal distribution with a constant fractional standard deviation. The fluctuation of each neutron count was simulated by changing all the elements of matrix **X** as follows:

$$x'_{jk} = x_{jk}(1 + \alpha N_\xi), \tag{32}$$

where α is the fractional standard deviation and N_ξ is the random number sampled from the standard normal distribution. Using a matrix whose element was x'_{jk}, the fundamental mode eigenvalue γ_0 was computed using DMD. This trial was repeated 300 times for $\alpha =$ 0.01 and

0.001. When the fractional standard deviation α is 0.01 or 0.001, the corresponding neutron counts at each data point are 10,000 and 1,000,000, respectively. The sample mean, sample standard deviation, and standard error of γ_0 are listed in Table 4. The sample means of γ_0 were significantly underestimated when compared with γ_0 obtained from the data without uncertainty. That is, γ_0 is biased and does not distribute around the true value if each data fluctuates owing to measurement uncertainty. The bias increased with the fractional standard deviation, α. The bias is caused by many factors such as the influence of the higher harmonics and the capability of the DMD for the flux distribution including the higher harmonics. Thus, the mechanism of the underestimation (or overestimation) is too complicated to identify the reason of the bias.

Table 4 Fundamental mode γ-eigenvalues of DMD

	γ_0 (cm^{-1})			
	Exact	$\alpha = 0$	$\alpha = 0.01$	$\alpha = 0.001$
Sample mean	0.07113	0.07119*	0.06951	0.07099
Sample standard deviation	NA	NA	0.00181	0.00066
Standard error	NA	NA	0.00010	0.00004

* Similar to Table 3.

5.2 Estimation from measurement

This section outlines a methodology to obtain the best estimate of the fundamental mode eigenvalue using measured data and DMD. After an exponential experiment is performed and the neutron flux distributions are measured, DMD is applied to compute the fundamental mode eigenvalue of the decay constant using the measured data. This process is repeated several times to obtain the sample mean. As shown in Section 5.1, this sample mean is biased owing to the statistical uncertainty in each measured data. If the ratio of the biased mean value to the true eigenvalue is known, the true eigenvalue can be deduced from the measurement. This study proposes a method for estimating the ratio by employing a numerical simulation.

After a numerical model that reproduces the exponential experiment is constructed, the

sample mean of the fundamental mode γ-eigenvalue is calculated using the same procedure as in Section 5.1. The numerical model should reproduce the measurement conditions as closely as possible. The fractional standard deviation α at each data point used in the numerical model must coincide with that in the measurement. In addition, the exact γ-eigenvalue is calculated for the numerical model. The calculation code for this numerical model can be a deterministic diffusion or transport code. The use of a Monte Carlo code should be avoided because of the statistical uncertainties involved in the calculation results, unless the uncertainties are much smaller than the measurement uncertainties. The exact γ-eigenvalue can be easily obtained by a buckling search mode calculation, as installed in CITATION code. If a buckling search mode calculation is unavailable, the exact value can be obtained by fitting a neutron flux in a region that is sufficiently distant from the neutron source.

Here, we assume that the ratio of the biased mean value to the true eigenvalue can be accurately approximated by the ratio from this numerical model. The true fundamental mode γ-eigenvalue γ_{est} is estimated as follows:

$$\gamma_{est} = \bar{\gamma}_m \frac{\gamma_e}{\bar{\gamma}_c}, \tag{33}$$

where $\bar{\gamma}_m$ is the sample mean of γ-eigenvalues from the measurement and DMD, γ_e is the exact γ-eigenvalue of the numerical model, and $\bar{\gamma}_c$ is the sample mean calculated using the procedure in Section 5.1.

5.3 Bootstrapping for exponential experiment

The procedure proposed in Section 5.2 requires the measurement of an exponential experiment to be repeated many times. A large number of repetitions is desirable to ensure a reliable and significant result. However, if each measurement requires considerable resources and the repetition times must be restricted, the data set obtained from the measurements may not be sufficiently large. In this section, bootstrapping (Efron, 1979; Endo and Yamamoto, 2019) is proposed to simulate sampling from a large population using a very limited number of repeated measurements. The bootstrapping procedure for the exponential experiment is illustrated in Fig.

16. First, an exponential experiment is repeated *N* times (e.g., $N = 3$ in Fig. 16). We have *N* data arrays for each horizontal position, as shown in the left figure in Fig. 16. Each data array is composed of a series of measured data along the vertical direction in a horizontal position. At each vertical position, one data is randomly selected from the *N* samples at the same vertical position. This procedure is performed for all vertical positions. Then, we have a new data array at this horizontal position. This procedure is performed for all horizontal positions. Finally, we have a new complete dataset for performing DMD, and we obtain a γ-eigenvalue for this dataset. This procedure is repeated *M* times, where *M* is much larger than the number of original samples *N*. The sample mean of the *M* number of γ-eigenvalues is used for $\bar{\gamma}_m$ in Eq. (33) with high reliability, even if a small number of repeated measurements are performed.

Bootstrapping was performed for the numerical model described in Section 5.1. Using Eq. (32), 10 data sets that simulated the measured data in the exponential experiment were generated for $\alpha =$ 0.01 and 0.001. Bootstrap samples were randomly selected from the 10 original datasets as illustrated in Fig. 16. DMD was applied to the bootstrap samples, and the bootstrap procedure was repeated 300 times. In Table 5, the sample mean and sample standard deviation that were generated from the bootstrap samples are compared with those of the actual sampling (300 trials), as presented in Section 5.1. As shown in Table 5, the results generated from the bootstrap samples are equivalent to the actual sampling. This numerical simulation suggests that bootstrapping is expected to simulate a larger number of exponential experiments from a limited number of measured data.

In an actual measurement, a measurement does not have to be repeated many times (e.g., 10 in this example) in order to obtain a multiple number of data sets. The multiple data sets for bootstrapping can be obtained by equally separating a measurement time assigned to each measurement point into the number of the data sets. Thus, the measurement is required to be performed only once.

Table 5 Fundamental mode γ-eigenvalues by actual sampling and bootstrapping

	γ_0 (cm^{-1})			
	$\alpha = 0.01$		$\alpha = 0.001$	
	Actual sampling*	Bootstrap	Actual sampling*	Bootstrap
Sample mean	0.06951	0.06939	0.07099	0.07099
Sample standard deviation	0.00181	0.00187	0.00066	0.00060

*The same as in Table 4

6. Conclusions

DMD is originally intended to be applied to time-dependent dynamic system analyses. An exponential experiment deals with the static mode of three-dimensional neutron flux distributions. However, DMD can be extended to an exponential experiment by considering the vertical coordinate as the time coordinate in the DMD. The snapshot at each time step in the DMD corresponds to a horizontal neutron flux profile at each vertical level. The fundamental mode γ-eigenvalue, γ_0, in an exponential experiment can easily be detected in a region that is sufficiently distant from the neutron source. Meanwhile, the flux distribution near the neutron source is mostly dominated by many higher harmonics, rendering determination of γ_0 difficult. Applying DMD to such a challenging situation easily and accurately extracted γ_0 from a flux distribution that was significantly affected by higher harmonics. In the numerical examples in this study, higher harmonics up to the third order were reproduced by DMD, although the objective of this study was to extract the fundamental mode. Generally, it is advantageous to horizontally and vertically collect numerous data points. The numerical examples in this study revealed that a fine resolution of data points in the vertical direction did not always yield better solutions. DMD yielded an accurate γ-eigenvalue for the fundamental mode and first-higher harmonic regardless of using a limited number of data points in the water reflector region.

If the statistical uncertainty of the measured neutron counts is considered, the DMD yields biased γ-eigenvalues instead of yielding equally distributed eigenvalues around the true value.

This study proposes a method to adjust the bias by performing numerical simulations for an exponential experiment. Hence, an exponential experiment should be performed many times to obtain an accurate measured mean value of the γ-eigenvalue. However, bootstrapping is a potent tool for simulating a large number of measurements by resampling from a very limited number of measured data.

Appendix

In this Appendix, the neutron source was placed at the node of the third-higher harmonic as shown in Fig. 17. The eigenvalues and eigenfunctions were obtained from the DMD method. The calculation conditions were the same as in Sec. 4.3.1 except the neutron source position. The eigenvalues are listed in Table 6. The third- and fourth-higher harmonics were not captured by the DMD method. The eigenfunction of the fifth higher-harmonic along the vertical line in Fig. 17 is shown in Fig.18 together with the solution of RHEINGOLD code. The DMD method yielded a rough reproduction of the fifth-higher harmonic.

Table 6 Eigenvalues of DMD from matrix of 133 × 29 and $r = 23$ (source at the node of the third-higher harmonic)

	Exact (cm^{-1})	DMD (cm^{-1})
γ_0	0.07113	0.07113
γ_1	0.1723	0.1722
γ_3	0.2324	—
γ_4	0.2584	—
γ_5	0.2602	0.2673

References

Abdo, M., Elzohery, R., Roberts, J.A., 2019. Modeling isotopic evolution with surrogates based on dynamic mode decomposition. Ann. Nucl. Energy 129, 280–288. https://doi.org/10.1016/j.anucene.2019.01.048.

Anderson, E., Bai, Z., Bischof, C., Blackford, S., Demmel, J., Dongarra, J., Du Crozm, J., Greenbaum, A., Hammarling, S., McKenney, A., Sorensen, D., 1999. LAPACK Users' Guide (Third). Philadelphia, PA: Society for Industrial and Applied Mathematics.

Di Ronco, A., Introini, C., Cervi, E., Lorenzi, S., Jeong, Y.S., Seo, S.B., Bang, I.C., Giacobbo, F., Cammi, A., 2020. Dynamic mode decomposition for the stability analysis of the Molten Salt Fast Reactor core. Nucl. Eng. Des. 362, 110529. https://doi.org/10.1016/j.nucengdes.2020.110529

Efron, B., 1979. Bootstrap methods: another look at the Jackknife. Ann. Stat. 7, 1–26. https://doi.org/10.1214/aos/1176344552.

Endo, T., Yamamoto, A., 2019. Comparison of theoretical formulae and bootstrap method for statistical error estimation of Feynman-α method. Ann. Nucl. Energy 124, 606–615. https://doi.org/10.1016/j.anucene.2018.10.032.

Fowler, T.B., Vondy, D.R., Cunningham, G.W., 1971. Nuclear Reactor Core Analysis Code: CITATION, ORNL-TM-2496, Rev. 2.

Hardy, Z.K., Morel, J.E., Ahrens, C., 2019. Dynamic mode decomposition for subcritical metal systems. Nucl. Sci. Eng. 193 1173–1185. https://doi.org/10.1080/00295639.2019.1609317.

Kutz, J.N., Brunton, S.L., Proctor, J.L., 2016. Dynamic mode decomposition: Data-driven modeling for complex systems, Society for Industrial and Applied Mathematics, Philadelphia, Pennsylvania.

McClarren, R.G., 2019. Calculating time eigenvalues of the neutron transport equation with dynamic mode decomposition. Nucl. Sci. Eng. 193, 854–867. https://doi.org/10.1080/00295639.2018.1565014.

McClarren, R.G., Haut, T.S., 2020. Data-driven acceleration of thermal radiation transfer calculations with the dynamic mode decomposition and a sequential singular value decomposition. arXiv preprint arXiv:2009.11686.

Roberts, J.A., Xu, L., Elzohery, R., Abdo, M., 2019. Acceleration of the power method with dynamic mode decomposition. Nucl. Sci. Eng. 193, 1371–1378.

https://doi.org/10.1080/00295639.2019.1634928.

Schmid, P.J., 2010. Dynamic mode decomposition of numerical and experimental data. J. Fluid Mech. 656, 5–28. https://doi.org/10.1017/S0022112010001217.

Suzaki, T., 1991. Subcriticality determination of low-enriched UO_2 lattices in water by exponential experiment. J. Nucl. Sci. Technol. 28, 1067–1077. https://doi.org/10.3327/jnst.28.1067.

Suzaki, T., Kurosawa, M., Hirose, H., Yamamoto, T., Nakajima, K., Kanaizuka, F., Kobayashi, I., Kaneko, T., 1995. Exponential experiments of PWR spent fuel assemblies for acquiring subcriticality benchmarks usable in burnup credit applications," Proc. Int. Conf. on Nucl. Criticality Safety, September 17-21, 1995, Albuquerque, New Mexico.

Suzaki, T., Suyama, K., Kaneko, T., 1999. Measurement of criticality properties of a BWR spent fuel assembly. Proc. Int. Conf. on Nucl. Criticality Safety, September 20-24, 1999, Versailles, France.

Tsuruta, H., Kobayashi, I., Suzaki, T., Ohno, A., Murakami, K., Matsuura, S., 1978. Critical sizes of light-water moderated UO_2 and PuO_2-UO_2 lattices. Japan Atomic Energy Research Institute, JAERI-1254.

Yamamoto, T., Miyoshi, Y., Tonoike, K., Okamoto, H., Ida, T., Aoki, S, 2003. Effect of higher-harmonics flux in exponential experiment for subcriticality measurement. J. Nucl. Sci. Tehcnol. 40, 77–83. https://doi.org/10.1080/18811248.2003.9715336.

Yamamoto, T., Miyoshi, Y., 2003. An algorithm of α- and γ-mode eigenvalue calculations by Monte Carlo method. Proc. 7th Int. Conf. on Nuclear Criticality Safety (ICNC'03), JAERI-Conf 2003-019, Japan Atomic Energy Research Institute, Tokai, Japan, October 2003.

Yamamoto, T., 2012. Monte Carlo algorithm for buckling search and neutron leakage-corrected calculations. Ann. Nucl. Energy 47, 14–20. https://doi.org/10.1016/j.anucene.2012.04.017.

Yamamoto, T., Sakamoto, H., 2019a. Two-step Monte Carlo sensitivity analysis of alpha- and gamma-eigenvalues with the differential operator sampling method. Ann. Nucl. Energy 133, 100–109. https://doi.org/10.1016/j.anucene.2019.05.013.

Yamamoto, T., Sakamoto, H., 2019b. Decomposition of neutron noise in a reactor into higher-

order mode components and investigation of the space and frequency dependence. Prog. Nucl. Energy 117, 103098. https://doi.org/10.1016/j.pnucene.2019.103098.

List of figures

Fig. 1 Schematic overview of DMD application to an exponential experiment.

Fig. 2 Horizontal view of exponential experiment, mesh configuration, and 133 data points.

Fig. 3 Schematic elevation view of exponential experiment.

Fig. 4 Thermal flux distributions in vertical direction at A, B, and C.

Fig. 5 Sixteen data points used for DMD.

Fig. 6 Local spatial decay constant γ and the exact constant at A, B, and C.

Fig. 7 Schematic of higher harmonics up to 5th order and γ-eigenvalues.

Fig. 8 Decomposed higher harmonics along the diagonal at 5 cm above neutron source.

Fig. 9 Vertical distributions of higher harmonics at A.

Fig. 10 Fundamental mode thermal flux by DMD and exact flux along diagonal (133 points).

Fig. 11 First-harmonic thermal flux by DMD and exact flux along diagonal (133 points).

Fig. 12 Third-harmonic thermal flux by DMD and exact flux along diagonal (133 points).

Fig. 13 Fundamental mode thermal flux by DMD and exact flux along diagonal (16 points).

Fig. 14 First-harmonic thermal flux by DMD and exact flux along diagonal (16 points).

Fig. 15 Third-harmonic thermal flux by DMD and exact flux along diagonal (16 points).

Fig. 16 Example of bootstrapping for exponential experiment. $C_{m,n}$: neutron count at mth elevation and nth measurement at a horizontal position.

Fig. 17 Horizontal view of the numerical example where the neutron source was placed at the node of the third-higher harmonic.

Fig 18 Fifth-harmonic thermal flux by DMD and exact flux.

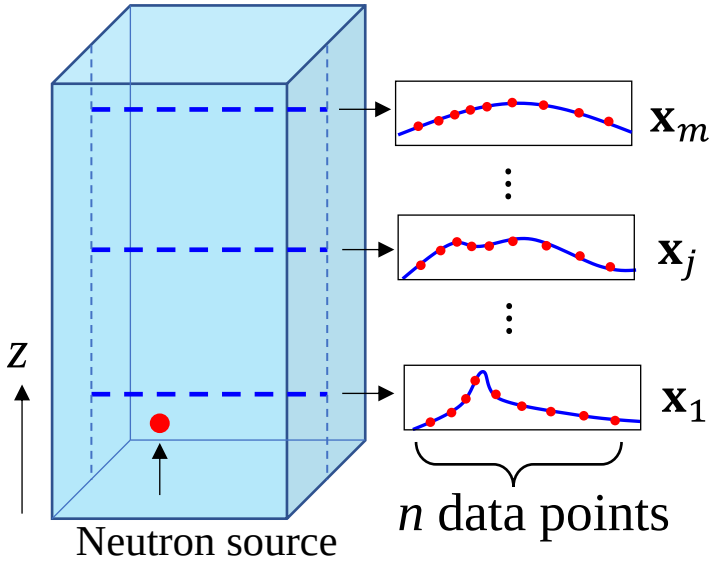

Fig. 1 Schematic overview of DMD application to an exponential experiment.

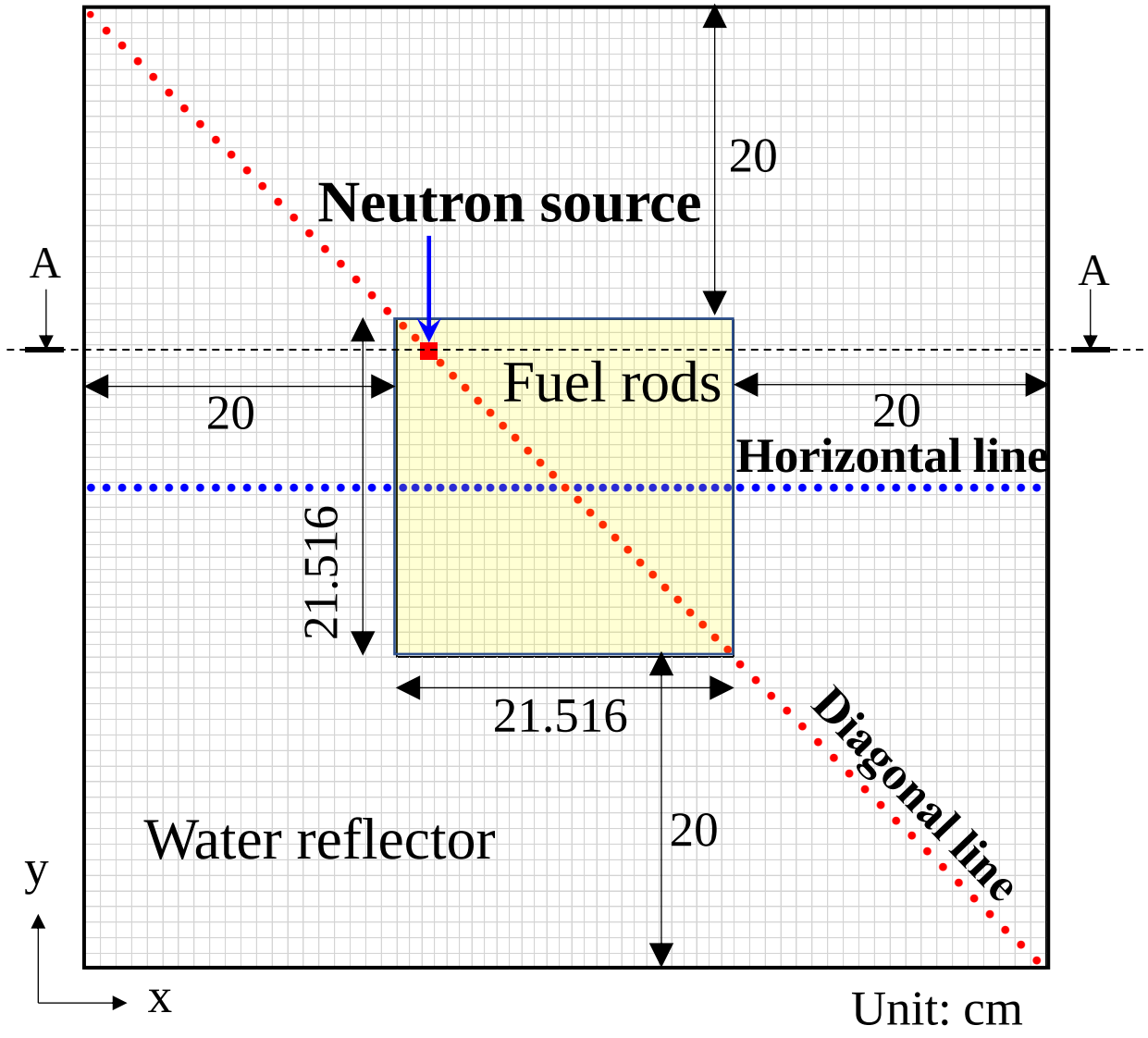

Fig. 2 Horizontal view of exponential experiment, mesh configuration, and 133 data points.

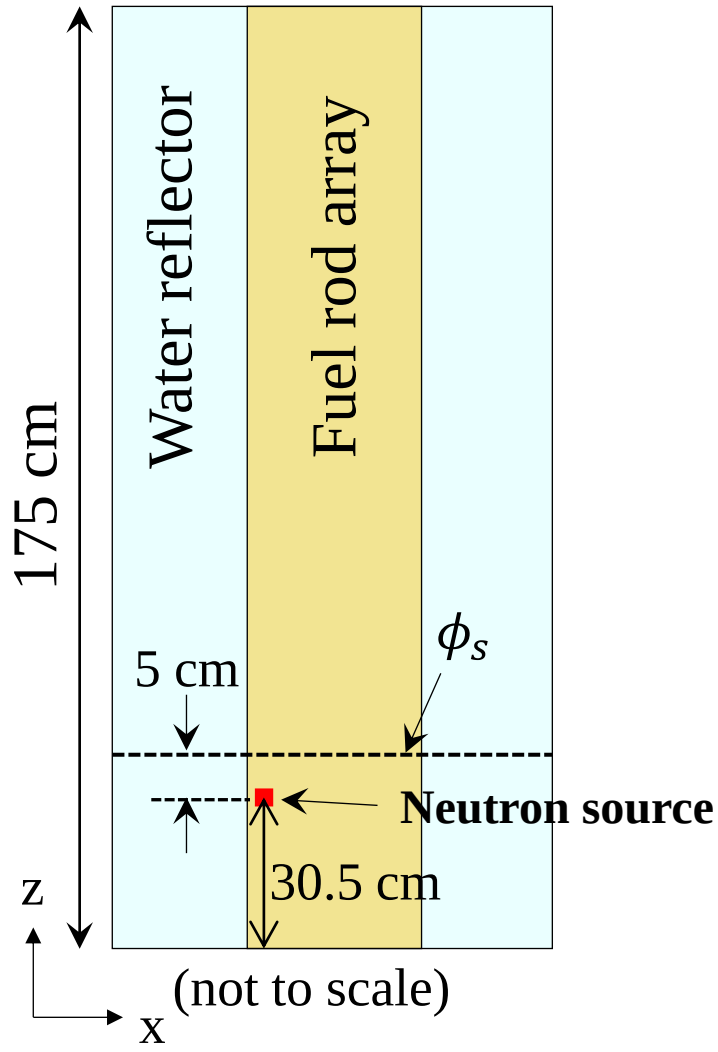

Fig. 3 Schematic elevation view of exponential experiment.

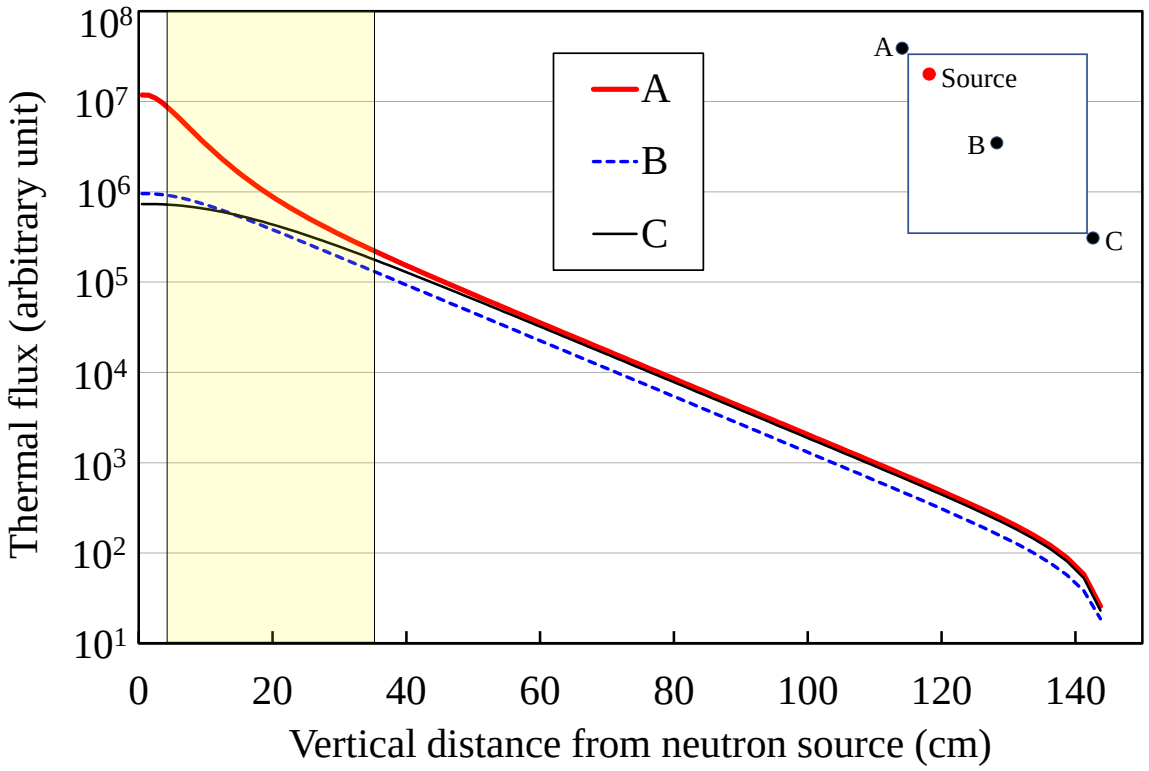

Fig. 4 Thermal flux distributions in vertical direction at A, B, and C.

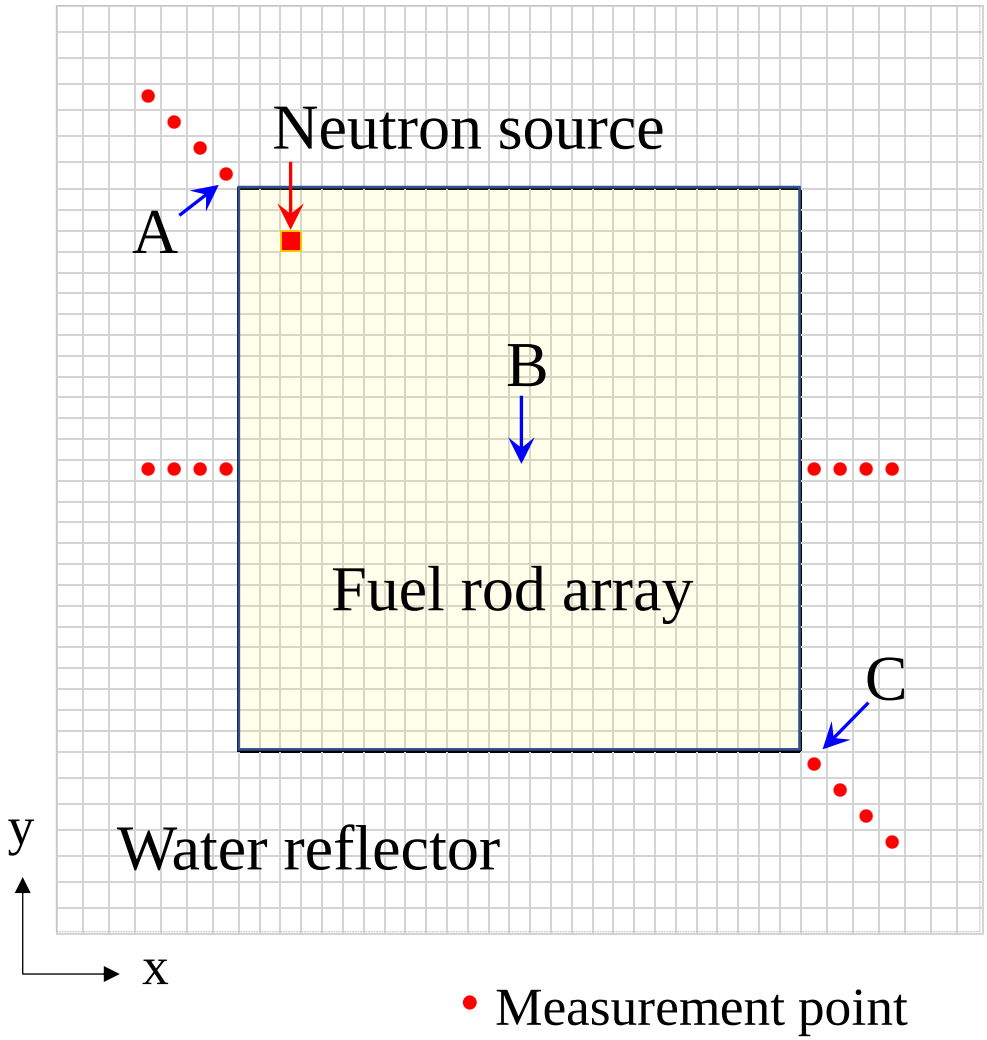

Fig. 5 Sixteen data points used for DMD.

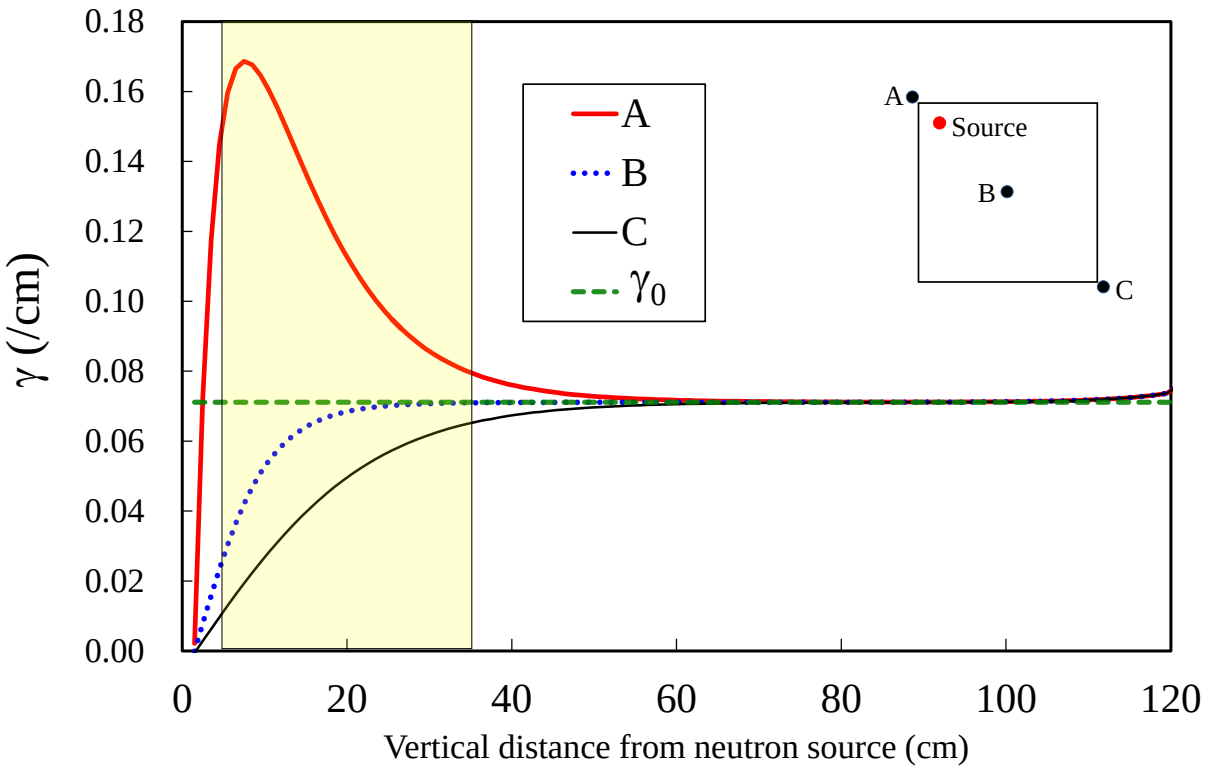

Fig. 6 Local spatial decay constant γ and the exact constant at A, B, and C.

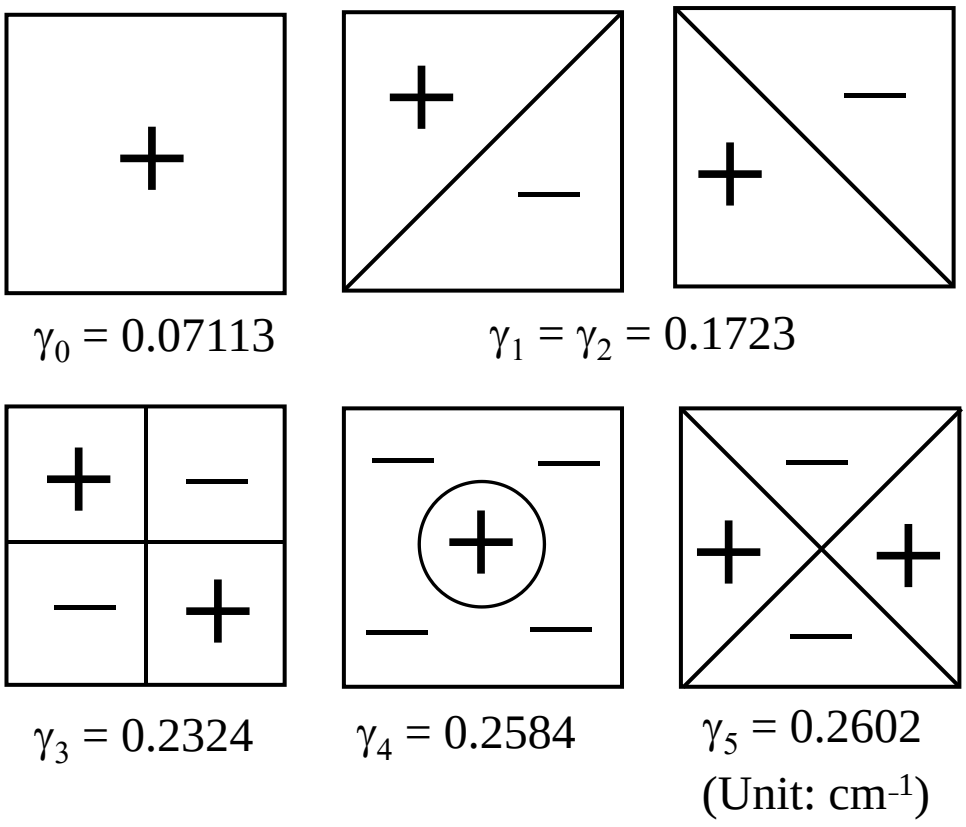

Fig. 7 Schematic of higher harmonics up to 5th order and γ-eigenvalues.

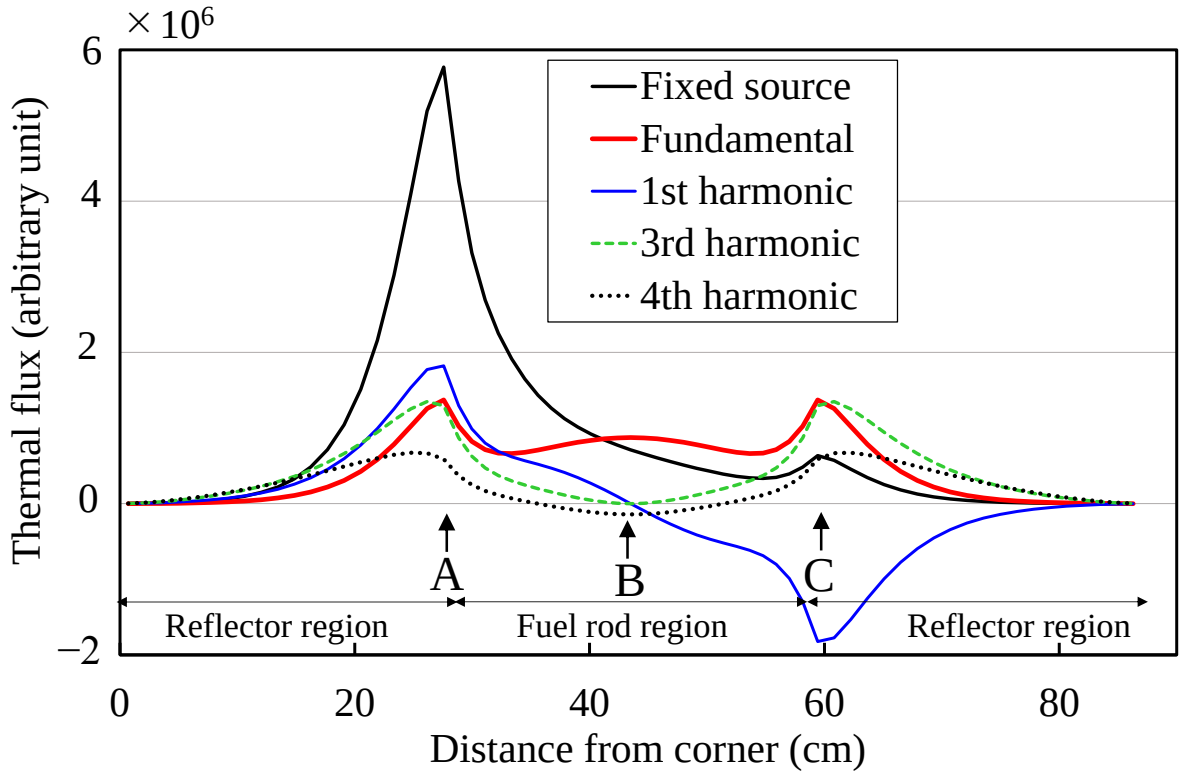

Fig. 8 Decomposed higher harmonics along the diagonal at 5 cm above neutron source.

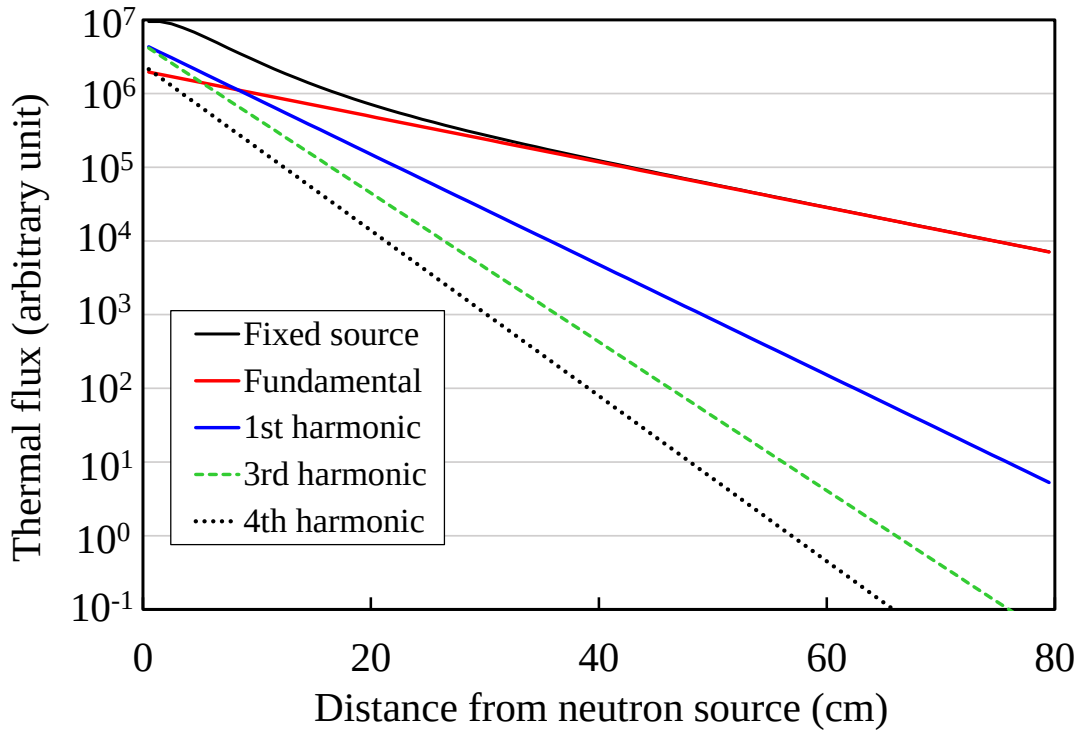

Fig. 9 Vertical distributions of higher harmonics at A.

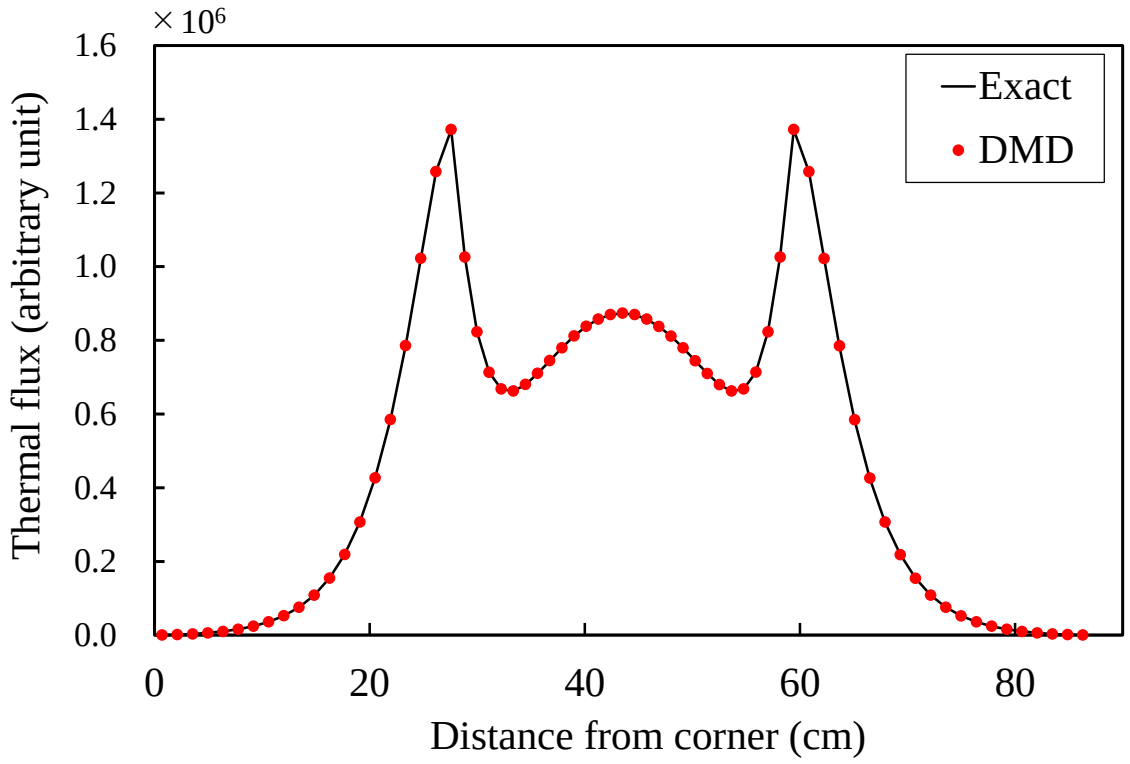

Fig. 10 Fundamental mode thermal flux by DMD and exact flux along diagonal (133 points).

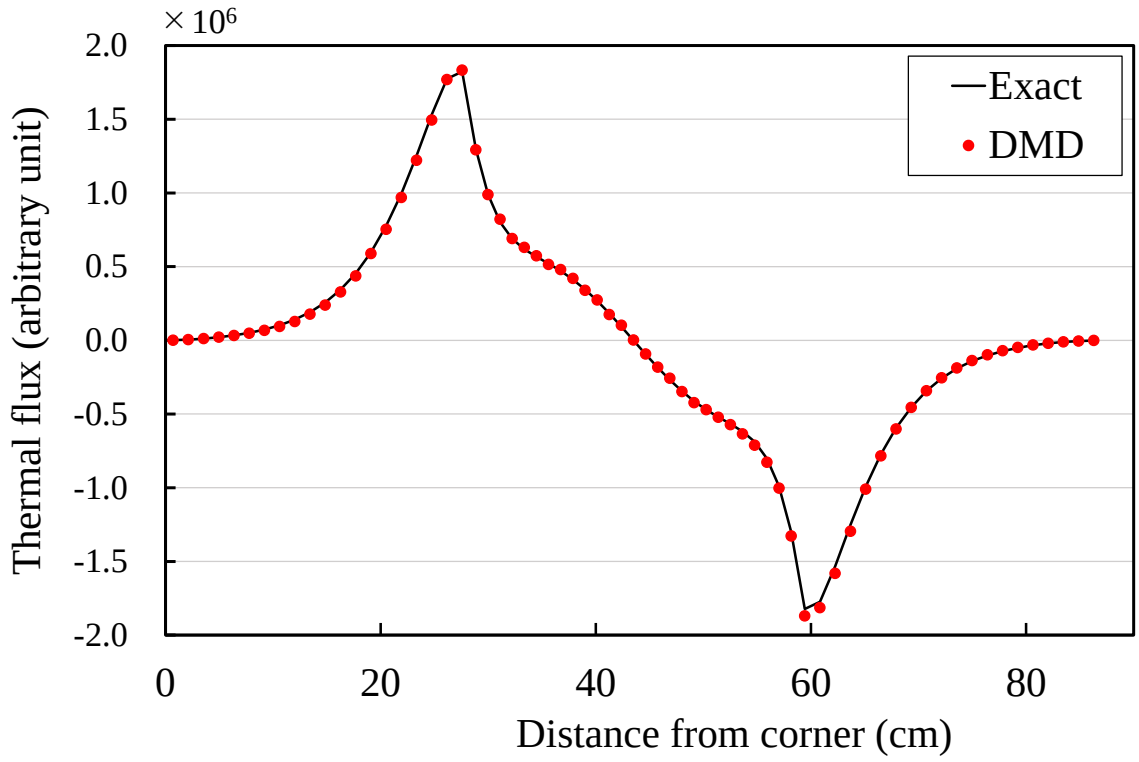

Fig. 11 First-harmonic thermal flux by DMD and exact flux along diagonal (133 points).

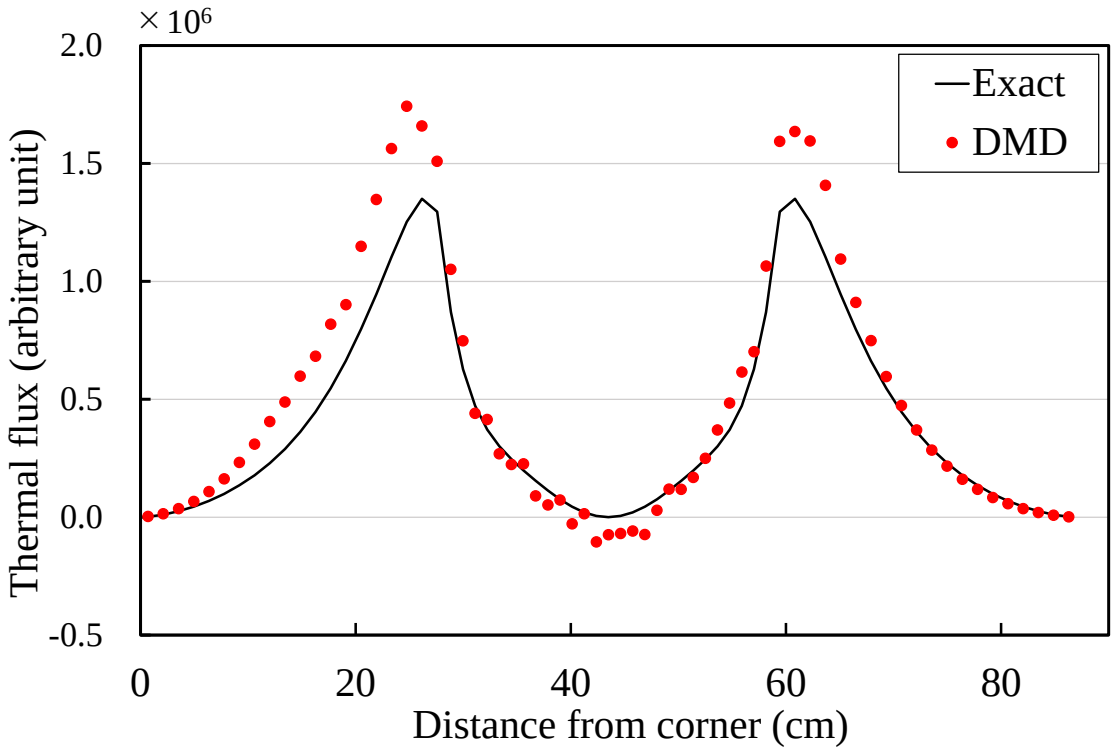

Fig. 12 Third-harmonic thermal flux by DMD and exact flux along diagonal (133 points).

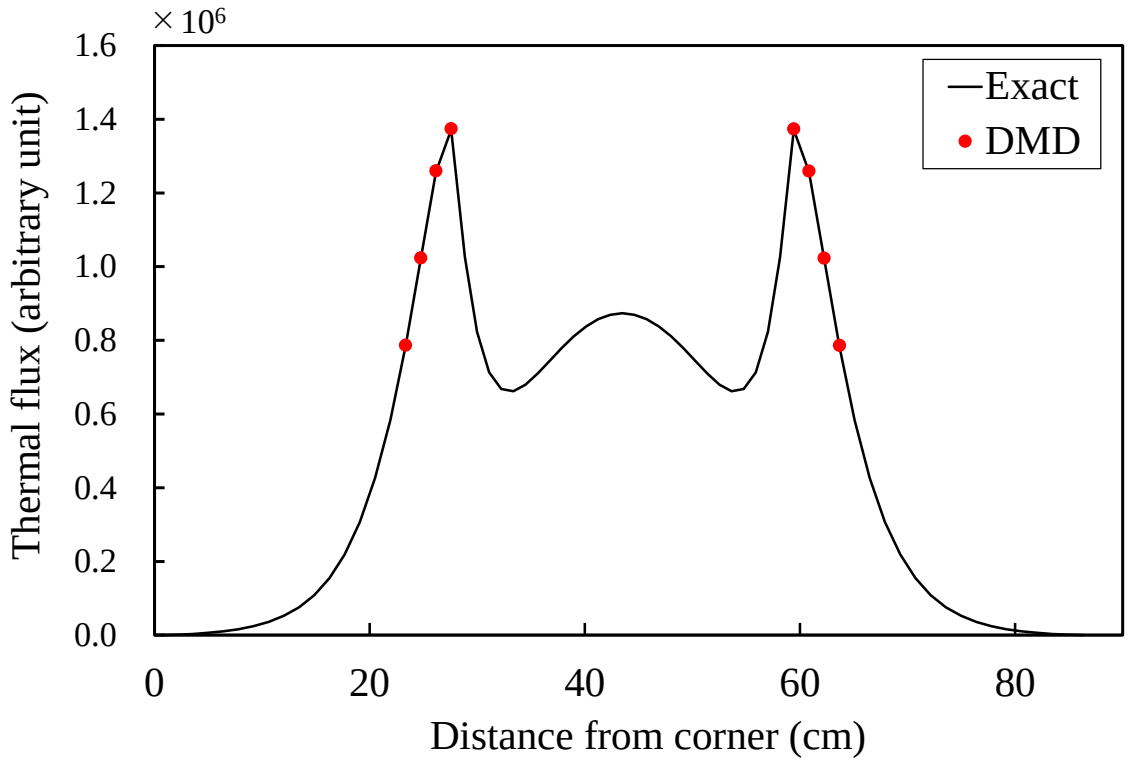

Fig. 13 Fundamental mode thermal flux by DMD and exact flux along diagonal (16 points).

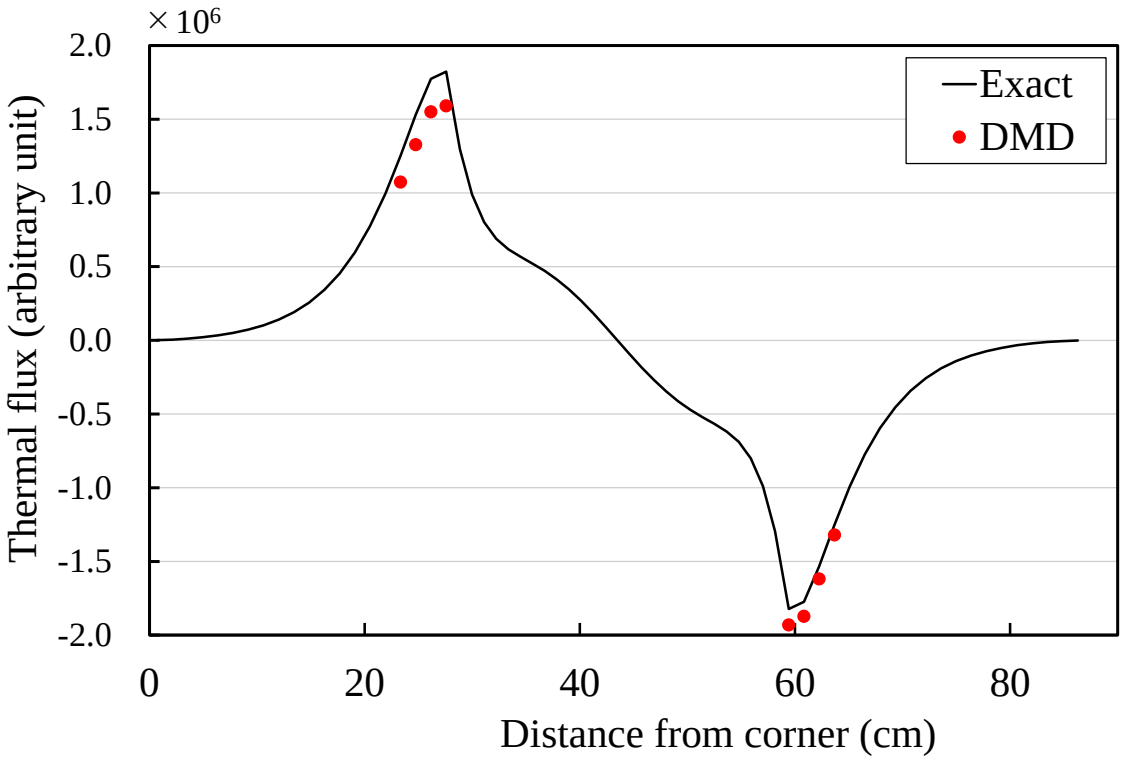

Fig. 14 First-harmonic thermal flux by DMD and exact flux along diagonal (16 points).

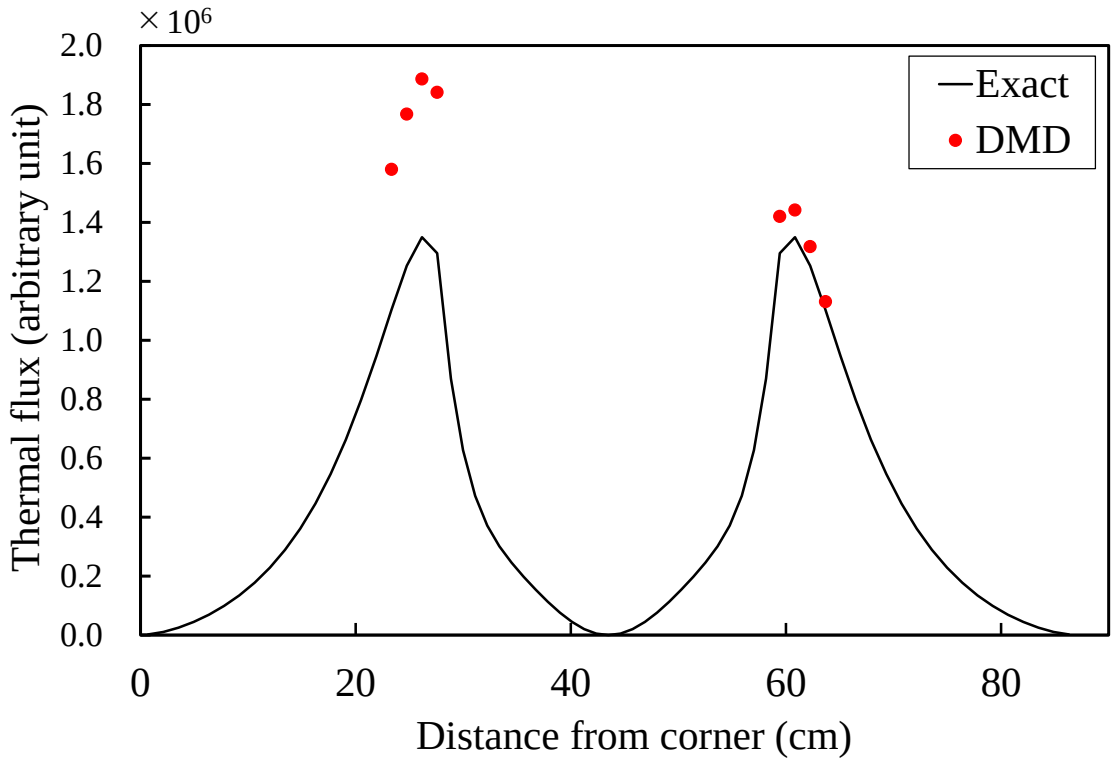

Fig. 15 Third-harmonic thermal flux by DMD and exact flux along diagonal (16 points).

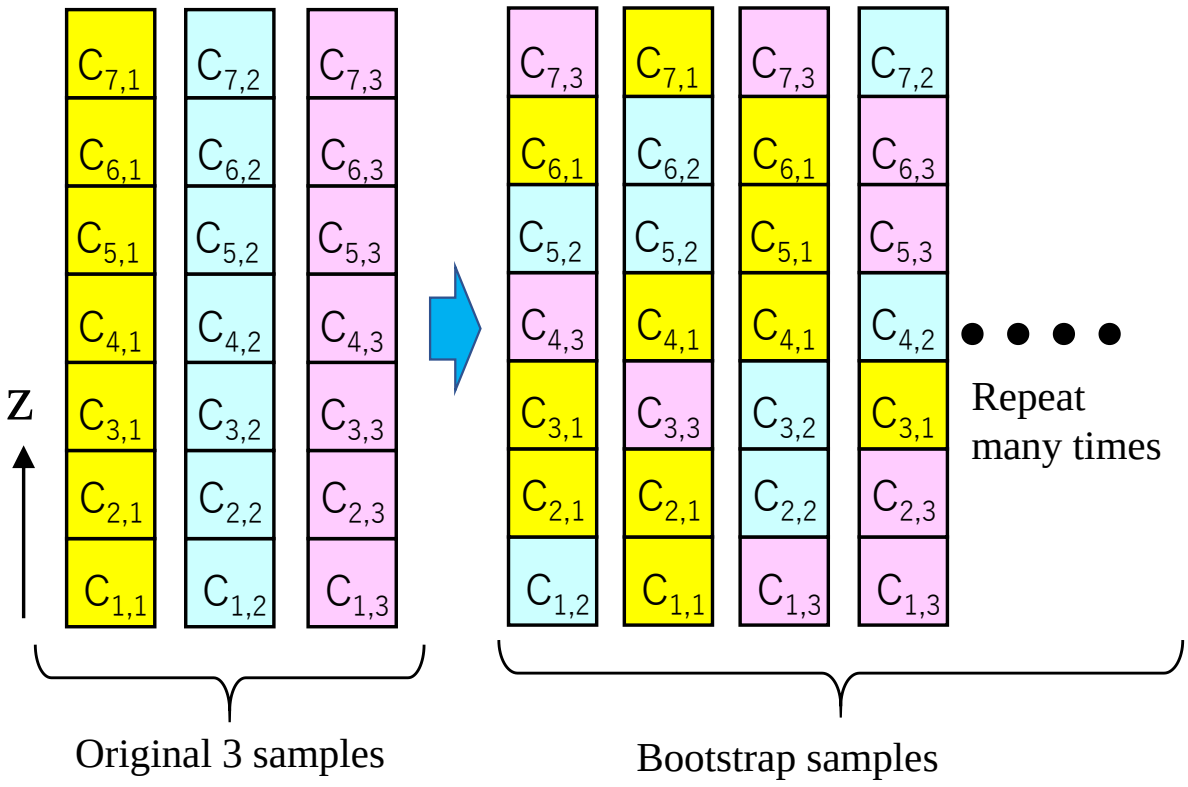

Fig. 16 Example of bootstrapping for exponential experiment. $C_{m,n}$: neutron count at *m*th elevation and *n*th measurement at a horizontal position.

1

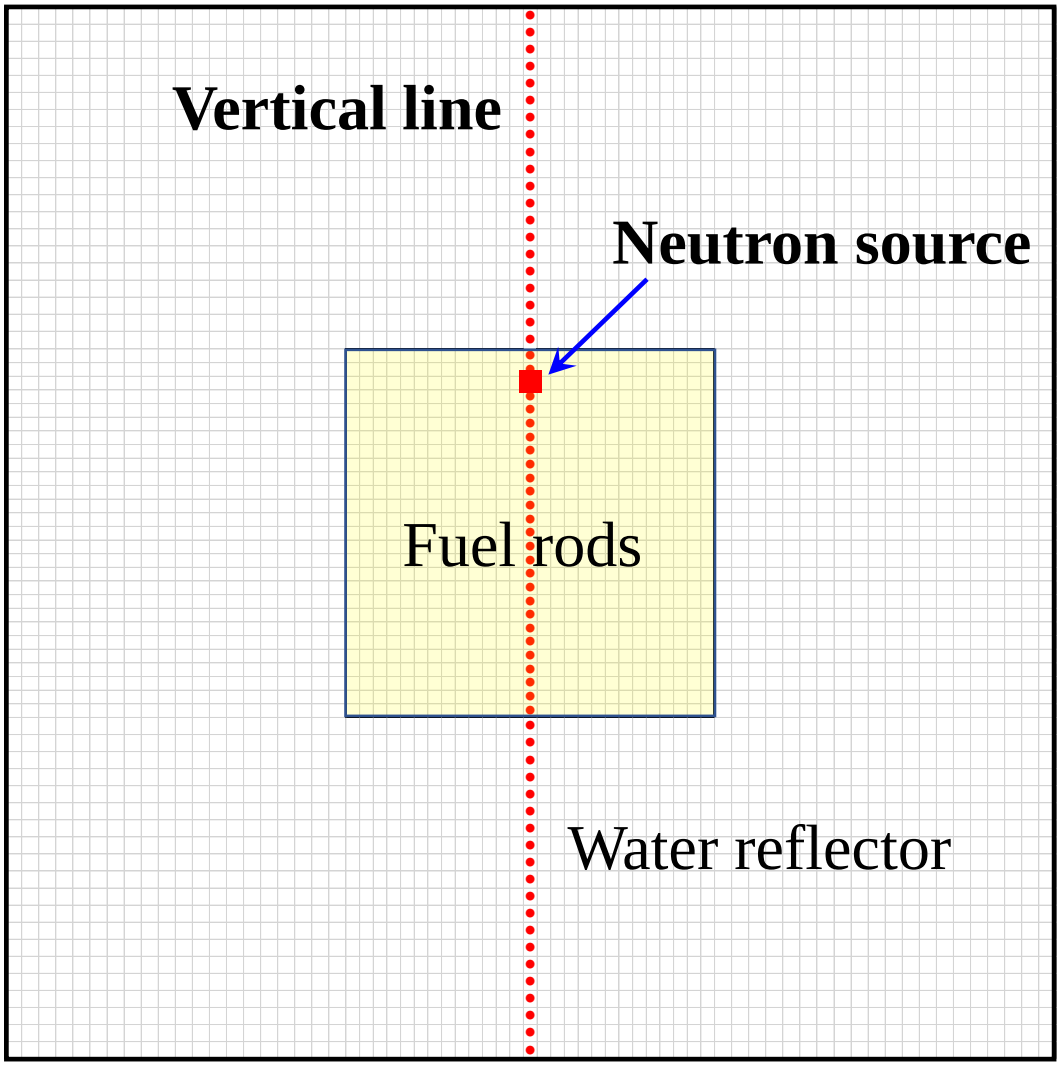

Fig. 17 Horizontal view of the numerical example where the neutron source was placed at the node of the third-higher harmonic.

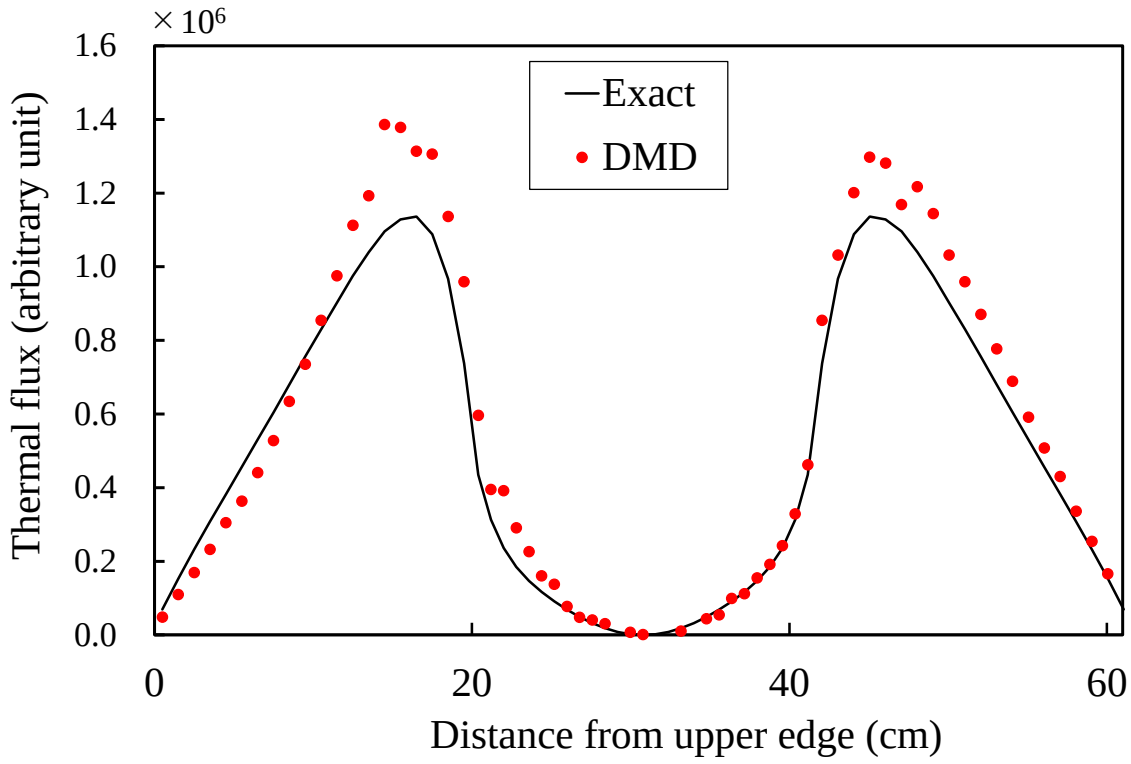

1 Fig 18 Fifth-harmonic thermal flux by DMD and exact flux.

CRediT authorship contribution statement

Toshihiro Yamamoto: Supervision, Methodology, Conceptualization, Investigation, Writing - original draft. **Hiroki Sakamoto**: Software, Validation, Formal analysis, Data curation, Writing - review & editing.

Declaration of interest statement

The authors declare no conflicts of interest associated with this manuscript.